



OPEN

Deposition, microstructure and nanoindentation of multilayer Zr nitride and carbonitride nanostructured coatings

Anwar Ul-Hamid

Nitrides, carbides, and carbonitrides of transition metal elements like Zr, W, Ti, etc. are generally employed to produce hard coatings. Zirconium-based hard coatings have shown useful applications in the areas of tribology, biomedicine and electrical due to their high thermal stability, hardness, biocompatibility, good erosion, wear, and corrosion resistance. In this study, we created homogeneous and tenacious nanostructured hard coatings based on Zr with good mechanical properties. The magnetron sputter deposition technique was utilized to coat stainless steel 316L substrates with multilayers of Zr/ZrN and ZrN/ZrCN with individual layer thicknesses of 250 and 500 nm for each coating composition. The deposition conditions were adjusted to create two different coating thicknesses of 2 and 3 μm . The thickness of the coating was confirmed using Calotest and the coatings' morphology and elemental composition were determined utilizing the atomic force microscope and scanning electron microscope equipped with energy dispersive x-ray spectrometer. Coating thickness and adhesion were measured using cross-sectional samples and XRD was utilized to analyze the coatings structure. Nanoindenter was employed to determine the instrumental nanoindentation hardness and elastic modulus. The influence of coating thickness on tribological behavior was further investigated using the ratio of nanohardness-to-elastic modulus (H/E). No evidence of decohesion was observed at the substrate/coatings interface, and the grains of all the coatings were observed to show columnar growth which were homogeneous, compact and dense. The grains of the ZrN/ZrCN coatings were observed to be denser, finer and more compact compared to those of the Zr/ZrN coatings. Correspondingly, higher hardness, modulus and H/E values were exhibited by ZrN/ZrCN than Zr/ZrN coatings. This suggests that the ZrN/ZrCN coatings are capable of exhibiting better wear resistance and fracture toughness. The coatings developed in this investigation are anticipated to be suitable for applications in tribology due to their excellent hardness and H/E properties.

Biomedical implants, household products, gas turbine engine components, and drilling and cutting equipment, are products used in industries such as the oil & gas, power, manufacturing, defense, and medicine, and are normally coated with wear resistant hard coatings in order to extend their service lifetimes. Transition metal carbides, nitrides, and carbonitrides based on Ti, Zr, W, and others, are commonly used in developing hard coatings. Because of their low vapour pressure & high melting point, coatings that are based on zirconium (Zr) are difficult to layer, and they are vulnerable to getting contaminated by carbon and oxygen during the process of deposition. This is presumably the reason for the paucity of studies in the literature on coatings based on Zr. Because of the bonding nature and structure of Zr, thin films based on Zr have high microhardness, excellent biocompatibility, high thermal stability, and excellent wear, erosion, corrosion & oxidation resistance. As a result, they are perfect for applications in tribology, biomedical, corrosion-resistant, electrical, nuclear fuel and decorative applications. Several aspects of ZrN coatings have been studied for a variety of applications. ZrN has been used in tribological applications for microhardness, adhesion and wear resistance, as well as integrated circuits barrier materials¹⁻²², anti-erosion materials for turbines & compressor blades²³⁻²⁵, electrical & optical properties^{26,27}, biocompatible materials²⁸, compatible materials for nuclear fuel elements²⁹⁻³¹, microstructure, composition, anti-corrosion and orientation-dependent materials³²⁻⁴⁰. Researches on the effect of synthesis factors on coating characteristics

Core Research Facilities, King Fahd University of Petroleum & Minerals, Dhahran 31261, Saudi Arabia. email: anwar@kfupm.edu.sa

have also been reported^{41–46}. The number of studies on ZrCN coatings in the literature are limited. Among the properties and applications explored for ZrCN are morphology, crystallinity & composition⁴⁷, oxidation and corrosion resistance^{48,49}, tribological⁵⁰, synthetic parameters⁵¹, biomedical^{52–59}, characterization⁶⁰ and optical⁶¹. The hardness of a given coating is affected by the method of synthesis technique, processing, elemental, coating structure and elemental composition. Because of the influence of the underlying substrate, measuring the hardness of thin coatings is difficult. Nanoindentation is a technique for evaluating thin coatings with small indenters under low stress and penetration depths of tens to hundreds of nanometers. Without perceiving or quantifying the size of the indent, the mechanical properties of the coatings can be determined. The values of elastic modulus and nanoindentation hardness are extracted using analytical models. The microstructures, properties and characterization of single-layer Zr, ZrN and ZrCN deposited by magnetron sputtering have been reported, and ZrN was said to exhibit the highest elastic modulus and hardness while Zr exhibited the least⁶¹.

Multilayer coatings, especially the ones composed of sub-layers of thicknesses in the nanometer range have been reported to show improved properties over the single layer ones^{62–69}. The properties and microstructure of a multilayer Zr/CrN coatings grown by the multi-arc ion plating method have been reported⁷⁰. Braic et al.⁷¹, developed a super lattice TiAlN/TiAlZrN multilayer coatings of different bilayer periods deposited by cathodic arc method and investigated their performances as wear resistant coatings. The tribological, mechanical, microstructural and microchemical properties of TiN/ZrN multilayer coatings with different bilayer periods and thicknesses have been reported⁷². Recently, many laser-assisted manufacturing techniques for producing multilayer coatings have been used with greater flexibility of control^{73,74}. Multilayer nitride coatings of TiN/TiAlN and Ti/TiN/TiAlN have been investigated for biomedical applications⁷⁵. Because of its cost effectiveness and reproducibility, the magnetron sputter deposition technology is widely used in industry⁷⁶. It generates adherent and uniform coatings and uses low deposition temperature, which allows for the creation of coatings with improved properties.

Using the magnetron sputter deposition process, multilayer coatings based on Zr/ZrN and ZrN/ZrCN each of layer thicknesses 250 and 500 nm and coatings thicknesses of 2 and 3 µm were synthesized in this study. SEM equipped with energy dispersive x-ray spectroscopy, atomic force microscopy, and x-ray diffraction were employed to investigate the surface morphology and structure of the coatings. The nanoindentation method was used to measure the mechanical properties; modulus and nanoindentation hardness. The indentation hardness was determined as a function of normal load using the load displacement curve. The effects of the coating thickness and adding of carbon on the coatings properties were also investigated.

Materials and methods

Coating synthesis. Magnetron sputter deposition was used to develop multilayer Zr/ZrN and ZrN/ZrCN coatings (total thickness 2 and 3 µm) on (100) Si wafers and stainless steel SS316L substrates (of 16 mm diameter disc, thickness 3 mm). The coatings' cross-sectional fracture morphology was next studied from broken coated Si wafers. The stainless steel substrates were polished with emery paper (ranging from 240 to 2400 grit) before being mirror-polished with a diamond suspension prior to deposition. The samples were cleaned ultrasonically using distilled water, ethanol, and acetone for ten minutes. Following that, in-situ sputter etching was carried out for 900 s at Ar pressure of 1.32 Pa and a steady current of 480 mA. As described by Silva et al.⁷⁷, unbalanced dual magnetron sputtering was used to create the coatings. Two highly pure (99.2%) 200 × 100 mm² Zr targets (rectangular in shape) mounted on unbalanced type-2 magnetrons were used to deposit the coatings in a reactive mode in an atmosphere of Ar/N₂/C₂H₂. For compositional and morphological characterization, the films were deposited onto (100) silicon wafers, as well as onto 316L stainless steel discs with a diameter of 3 mm. As previously described⁷⁸, the substrates were mounted in a matrix-like formation on a rotatable substrate holder. The parameters for creating multilayer Zr/ZrN and ZrN/ZrCN were chosen on the basis of each coating's deposition rates, adhesion properties, and composition. During the depositions, the bias voltage, chamber temperature and argon flux were respectively kept constant at –50 V, 100 °C and 60 sccm, while the current density of Zr was set between 1.8 and 2.0 A/cm². Table 1 shows the values for the target's potential, working & base pressures with some other deposition parameters used to deposit the final coatings.

Materials characterization. The surface morphology of coatings was investigated by undertaking high resolution secondary electron imaging of the coatings in their as-received state using field emission scanning electron microscope (FESEM, model TESCAN LYRA 3) equipped with an energy dispersive x-ray spectrometer from Oxford Inc. at an accelerating voltage of 20 kV. The backscattered electron images (BEI) and EDS spectra were collected using JEOL JSM-6610LV scanning electron microscope equipped with the energy dispersive x-ray spectrometer at an accelerating voltage of 10 kV. To avoid damaging the coating, the coated samples were cut with a slow-cutting diamond wheel and epoxy was used to mount them in cross-section. Later, the surface was ground with 600 grit silica carbide paper and polished using 1 µm diamond paste. In order to reduce charge build-up and improve the samples' surface conductivity during the SEM examination, a gold coater was utilized to sputter a thin layer of gold on the samples' surface in an argon atmosphere. Agilent 4500 series atomic force microscope (AFM) operated in a contact mode was also utilized to analyze the coatings' topography. The Rigaku Ultima IV x-ray diffractometer equipped with Ni-filtered Cu Kα radiation (λ = 0.154 nm) operated at 40 kV and 40 mA was utilized to assess the coatings phase composition from a range of 30 to 80° 2θ diffraction angle. The Scherrer equation was used to measure the average crystallite size.

$$D = \frac{k\lambda}{\beta \cos\theta}$$

where k is a constant (0.89), λ is x-ray wavelength (0.154 nm), β is peak broadening at full width half maximum (FWHM) in radians, and θ is the Bragg's diffraction angle.

Sample ID	Coating composition	Ø C ₂ H ₂ (sccm)	Ø N ₂ (sccm)	Time (s)	Base pressure (1 × 10 ⁻⁴ Pa)	Working pressure (Pa)	Zr Target-1 potential (V)	Zr Target-2 potential (V)	Substrate current (mA)
PN7	Zr ZrN	0	0 22	2940	3.9	0.49 0.57	298 341	341 400	242
PN8	Zr ZrN	0	0 22	4410	4.0	0.49 0.57	298 341	341 396	240
PN9	Zr ZrN	0	0 22	2940	4.0	0.49 0.57	298 333	337 380	270
PN10	Zr ZrN	0	0 22	4410	4.0	0.49 0.56	398 333	337 388	240
PN11	ZrN ZrCN	0 16	22 12	3024	4.7	0.53 0.55	349 361	404 451	280
PN12	ZrN ZrCN	0 16	22 12	4536	6.5	0.54 0.55	337 357	380 427	230
PN13	ZrN ZrCN	0 16	22 12	3024	4.0	0.53 0.55	337 361	384 435	230
PN14	ZrN ZrCN	0 16	22 12	4536	5.3	0.53 0.55	333 353	388 427	240

Table 1. Films deposition conditions.

N ₂ (sccm)	C ₂ H ₂ (sccm)	Zr (At. %)	N (At. %)	C (At. %)	O (At. %)	Deposition rate (µm h ⁻¹)
6	3.2	51.2 ± 1.9	25.1 ± 1.2	18.4 ± 0.7	5.3 ± 0.1	3.9
6	2.8	55.6 ± 3.9	23.6 ± 3.0	15.7 ± 0.3	5.1 ± 0.7	3.2
6	2.4	59.3 ± 2.3	21.1 ± 2.3	14.8 ± 0.0	4.7 ± 0.6	3.3
10	0	48.6 ± 5.1	43.2 ± 4.1	0.0 ± 0.0	8.2 ± 1.1	1.1
9	0	46.3 ± 1.5	44.9 ± 0.7	0.0 ± 0.0	8.8 ± 1.0	1.3
8	0	50.2 ± 1.9	40.5 ± 1.5	0.0 ± 0.0	9.3 ± 0.5	1.6

Table 2. Deposition conditions, EDS composition and deposition rates of the multilayer films used to determine the films deposition parameters.

Nanoindentation. The tests were carried out using CSM nanoindentation tester having a load range 0.5 to 300 mN. In order to ensure for limited volume penetration, a sharp three-faced pyramid Berkovich diamond tip was used. The tip of the nanoindentation tester was driven into the material at a constant load and speed for each nanoindentation. At an unload-load speed of 20 mN/min, indentations were done at loads of 10 and 20 mN. The loading and unloading cycles were separated by 60 s. The curve of load–displacement for each nanoindentation cycle was constructed by continuously monitoring the applied normal load and the displacement of the indenter tip. Hardness was evaluated using the indent's area, which was obtained using defined geometry and tip size. For determining elastic modulus and hardness, various analytical models have been developed, including the Joslin-Oliver technique^{79,80}, deformation energy technique^{81,82}, the Oliver and Pharr technique^{83,84}, the energy density technique⁸⁵, and the force indentation function technique^{86–88}. The Oliver and Pharr technique, used in this study, is the most popular of all the models.

The resistance to permanent deformation under a perpendicular stress is known as the nanoindentation hardness (H), and it is calculated as follows:

$$H = \frac{P_{max}}{A_p} \text{ Pascal.}$$

where P_{max} is the maximum perpendicular load, A_p is the projected contact area.

The elastic modulus (E) was computed from:

$$E = \frac{1 - \nu_s^2}{\frac{1}{E_\tau} - \frac{1 - \nu_i^2}{E_i}}$$

where E_i is the tip modulus, E_τ is the indentation contact's reduced modulus, ν_i is the tip Poisson's ratio and ν_s is the test sample Poisson's ratio.

Results and discussion

Coatings synthesis. To vary the amount of N & C-atoms in the coatings and identify the rate of deposition, the optimum composition, and evaluate the cross section morphology, appropriate parameters for creating Zr, ZrN, and ZrCN coatings were selected using thick multilayer films with various N₂ and C₂H₂ flows (Table 2). To determine the optimal synthesis parameters for achieving the best coating composition, thickness, and adhesion,

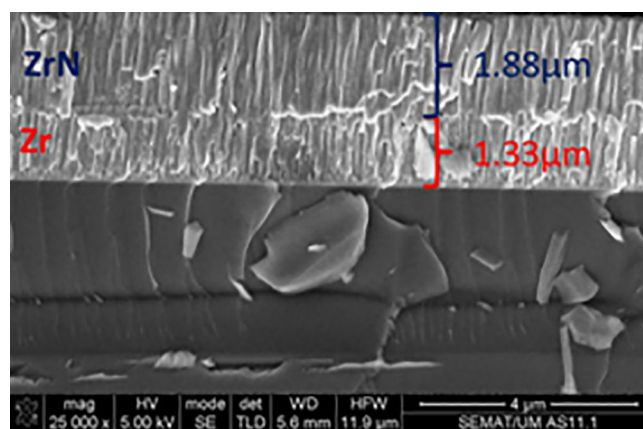


Figure 1. FESEM cross-section image of Zr/ZrN bilayer using a current density of 1.8 A with 0 and 11 sccm of nitrogen for Zr and ZrN.

Sample ID	Coating composition	Individual Layer thickness (nm)	$\text{O C}_2\text{H}_2$ (sccm)	O N_2 (sccm)	Time (s)	Grain size (nm)	Coating thickness (μm)	Deposition rate ($\mu\text{m h}^{-1}$)
PN7	Zr/ZrN	500	0	0–22	2940	12.6	1.96 ± 0.14	2.4 ± 0.2
PN8	Zr/ZrN	500	0	0–22	4410	12.7	3.22 ± 0.20	2.6 ± 0.2
PN9	Zr/ZrN	250	0	0–22	2940	8.50	2.12*	
PN10	Zr/ZrN	250	0	0–22	4410	9.25	2.96 ± 0.03	2.4 ± 0.0
PN11	ZrN/ZrCN	500	0–16	22–12	3024	5.96	2.02*	
PN12	ZrN/ZrCN	500	0–16	22–12	4536	5.55	3.00 ± 0.06	2.4 ± 0.1
PN13	ZrN/ZrCN	250	0–16	22–12	3024	8.50	2.02*	
PN14	ZrN/ZrCN	250	0–16	22–12	4536	9.25	2.99 ± 0.01	2.4 ± 0.0

Table 3. Films thicknesses, grain size and deposition rates. *Thicknesses and standard deviation are estimated using deposition rates calculated by means of calotest and SEM images.

the depositions were conducted in three series. The settings for depositing the 2nd and 3rd series of samples were chosen on the basis of the 1st series' optimization, with minor changes due to the usage of a new zirconium target, an excess of zirconium was detected. As a result, the zirconium current density was reduced and, in certain cases, gas fluxes were raised to obtain a thickness and composition identical to the first sample series. In order to alter the deposition conditions, Fig. 1 depicts the composition and thickness of two films deposited previously to the multilayer system. The target potential increased as gas fluxes increased; this increase is explained by the target surface's high reactivity with N_2 and C_2H_2 gases thereby poisoning surface of the target during reactive magnetron sputtering. The target potential of multilayer coatings varied, based on how much of gas is supplied to the reactor (Table 1). To obtain the requisite wear, the monolayers' thickness was measured utilizing the Calotest method, which involved spinning a 20 mm diameter sphere at 900 rpm for 120 s. Table 3 shows the results, whereas Fig. 1 shows a typical image for each composition. This test also provides a quantitative way to assess the films' adherence to the substrates. As a result, coatings that failed the test were removed, and deposition conditions were optimized to increase film adherence. Figure 2 illustrates an instance of failed film during the test. To increase adhesion, a zirconium interlayer was placed between the functional layer and the substrate for each coating composition, with thicknesses ranging from 250 to 300 nm.

The multilayer coating thicknesses were optimized making use of the monolayer thickness and SEM images in order to determine the deposition conditions of each compound. The coatings' cross-sectional FESEM views mostly exhibited columnar structures with a few small grains at the coating/alloy interface (Fig. 3). Such structure is distinctive of sputter-deposited coatings, which are formed at high super-saturation conditions, resulting in high rate of nucleation with tiny nuclei at the base^{89,90}. The primary columnar shape found in coatings explored here is a consequence of motion of grain boundary in the course of the epitaxial and coalescence developments. The Thornton model⁹¹, which proposes that faults from atomic shadowing & voided growths contribute to limited sample's surface diffusion, supports this type of growth. The columnar morphology for zirconium-based coatings have been documented extensively¹⁴. ZrN is a dazzling gold, whereas ZrCN is a dull gold and pure Zr coating is silver grey in color. This is consistent with previous findings of silver-colored metallic coatings containing high Zr and low nitrogen^{92,93}. The creation of stoichiometric ZrN, which has a gold color, occurs when the nitrogen content in the coatings rises^{44,92,93}. Additionally, Calotest was used to characterize the thickness of the multilayer where possible and the results are presented in Table 3. It must be stressed that Calotest allows the observation of the multilayer, as observed in Fig. 4, however the thickness of each individual layer was not calculated since the error of the technique may exceed the thickness of the individual layers. Figure 4 presents representative images

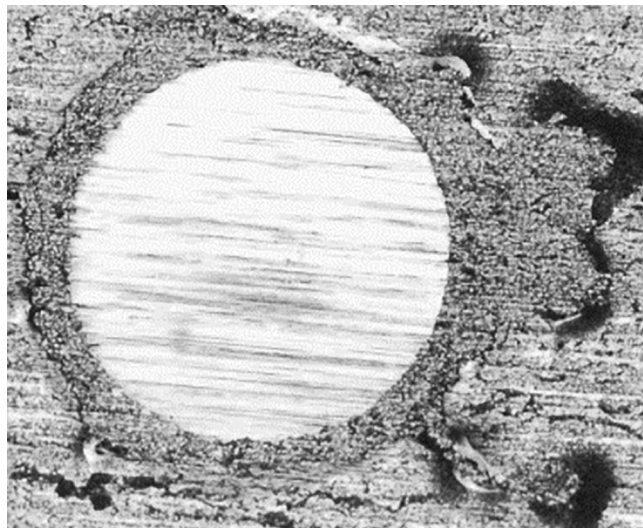


Figure 2. Calotest image of poorly adhered coating.

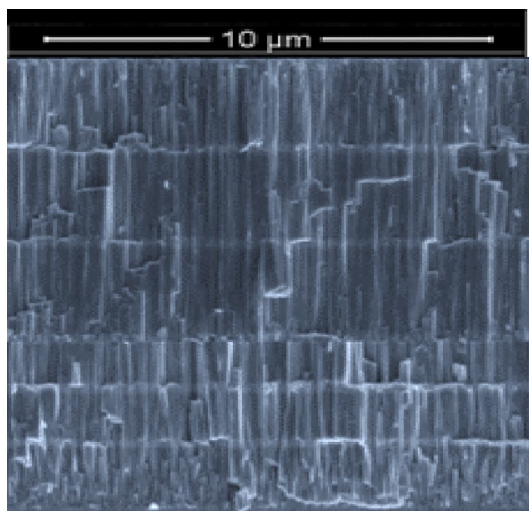


Figure 3. FESEM cross-section images of the deposited films.



Figure 4. Calotest images for (left image) PN14 at $\times 5$ and (right image) PN14 at $\times 50$.

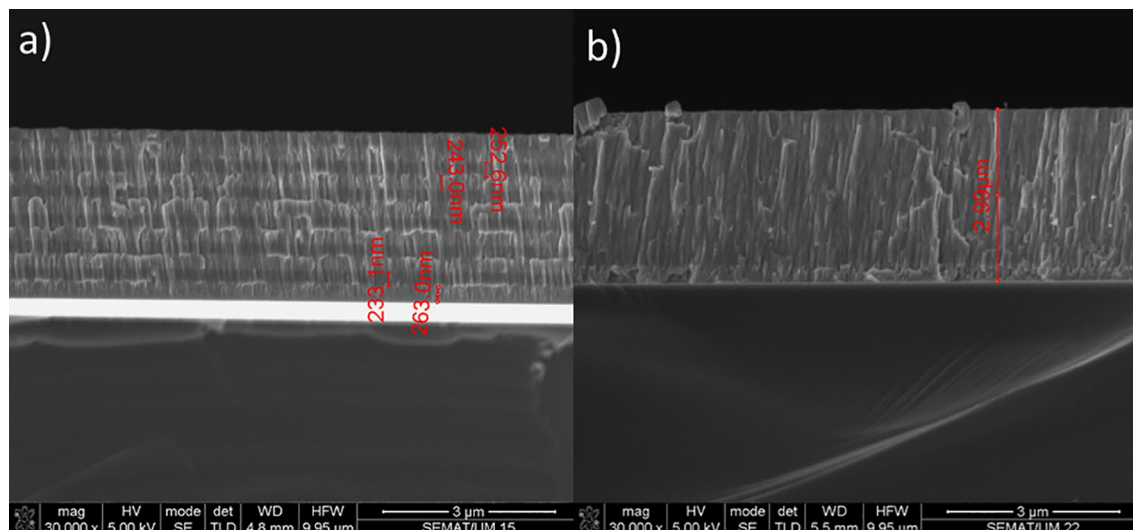


Figure 5. Cross-section FESEM images for samples (a) PN10 and (b) PN14.

of the multilayer for 250 of thickness of each individual layer. When nitrogen is added to the process, the film deposition rate decreases, as expected due to Zr targets' poisoning; however, when acetylene is used instead, the deposition rate increases, this is explained by carbon's ability to deposit directly into the films.

Multilayer cross-sectional SEM images are presented in Fig. 5 for two representative samples PN10 and PN14, corresponding to Zr/ZrN and ZrN/ZrCN multilayer, respectively. Figure 5a reveals a clear differentiation between the Zr and ZrN layer, with individual layer thicknesses close to 250 nm. This individual layer is not clearly noticed for the ZrN/ZrCN films, since structural and morphological changes for those materials are expected to be very subtle; nonetheless, the layer differentiation was detected by optical images after Calotest, as previously discussed. In contrast, Zr and ZrN may present different crystalline phases and the large compositional/morphology variation, as observed for surface SEM images and hence, each layer is clearly identified.

Materials characterization. *SEM/EDS.* The morphology of the coatings' top surfaces was studied using FESEM. The FESEM secondary electron micrographs of the coatings are shown in Fig. 6. The morphology of the coatings was essentially homogeneous, compact and dense with fine spherical grains. This is consistent with the previously observed columnar grain growth (Fig. 1). Aside from usual grain growth, localized grain growth near the thickening film's surface was seen, which was aided by nearby grain coalescence. Figure 6 demonstrates that for all coating compositions, coatings with a 3 μm thickness had larger grain sizes than those with a 2 μm thickness. The larger grain growth in the 3 μm coatings is attributed to the prolonged time of deposition, which may have allowed adjacent atoms to reorganize via surface diffusion, resulting in bigger grains. Generally, the grains of the ZrN/ZrCN coatings were more compact and smaller compared to those observed in the Zr/ZrN coatings. It has been reported that the carbon and nitrogen atoms in coatings that contain these atoms tend to limit grain growth by reducing neighboring grains' mobility, resulting in fine grain size⁷⁸, thus, resulting in the smaller grain size of the ZrN/ZrCN as compared to the Zr/ZrN coatings observed in this study. This is because carbon and nitrogen limit the mobility of adjacent grains and restrict them to the fine grains. Furthermore, densification of coatings was observed in the present study due to introduction of carbon and nitrogen. This leads to filling of interstitial positions due to diffusion of carbon and nitrogen which reduces the vacant sites, which in turn leads to more dense and smooth morphology of the coatings⁹³.

The cross-sectional backscattered electron image (BEI) of all coatings are shown in Fig. 7. It's clear that the deposition parameters used were successful in achieving the intended number of layers and thickness for each coating. The individual layers for each coating are of equal thickness. The Zr interlayer between the metal substrate and the functional layers is clearly visible (the first bright color) layer in all the coatings. The thickness of the Zr interlayer was 250 nm to 300 nm. The reason to insert Zr interlayer between substrate and functional layer is to improve their adhesion. The Zr interlayer is marked in Fig. 7. The coated samples exhibit well-defined multilayer structure with good planarity of individual layers and distinctive interfaces. For the Zr/ZrN multilayer coating, the alternating bright and grey color regions represent the Zr and ZrN layers respectively (Fig. 7a–d). While for the ZrN/ZrCN multilayer coatings, the alternating grey and dark color regions represent the ZrN and ZrCN layers respectively (Fig. 7e–h).

Figure 8 depicts representative cross-sectional EDS spectra for PN8 (Fig. 8a) & PN12 (Fig. 8b) and x-ray mapping for PN8 (Fig. 8c,d). EDS spectrum of PN8, whose result is representative of all the Zr/ZrN coatings, reveals a higher atomic mass % for Zr as compared to N with N to Zr ratio 0.835 (Fig. 8a). This is expected due to the presence of single Zr layers with the coatings. The error in the Zr and N was observed as 54.5 ± 1.85 and 45.5 ± 1.85 , respectively. The ZrN/ZrCN coatings, represented by the result for PN12 coating, exhibited an almost stoichiometric N to Zr ratio of 0.989 with the carbon atomic % almost twice the atomic % for either Zr or N (Fig. 8b). The error in the C, Zr and N was noted as 45.9 ± 2.38 , 27.2 ± 2.68 , and 26.9 ± 1.99 , respectively.

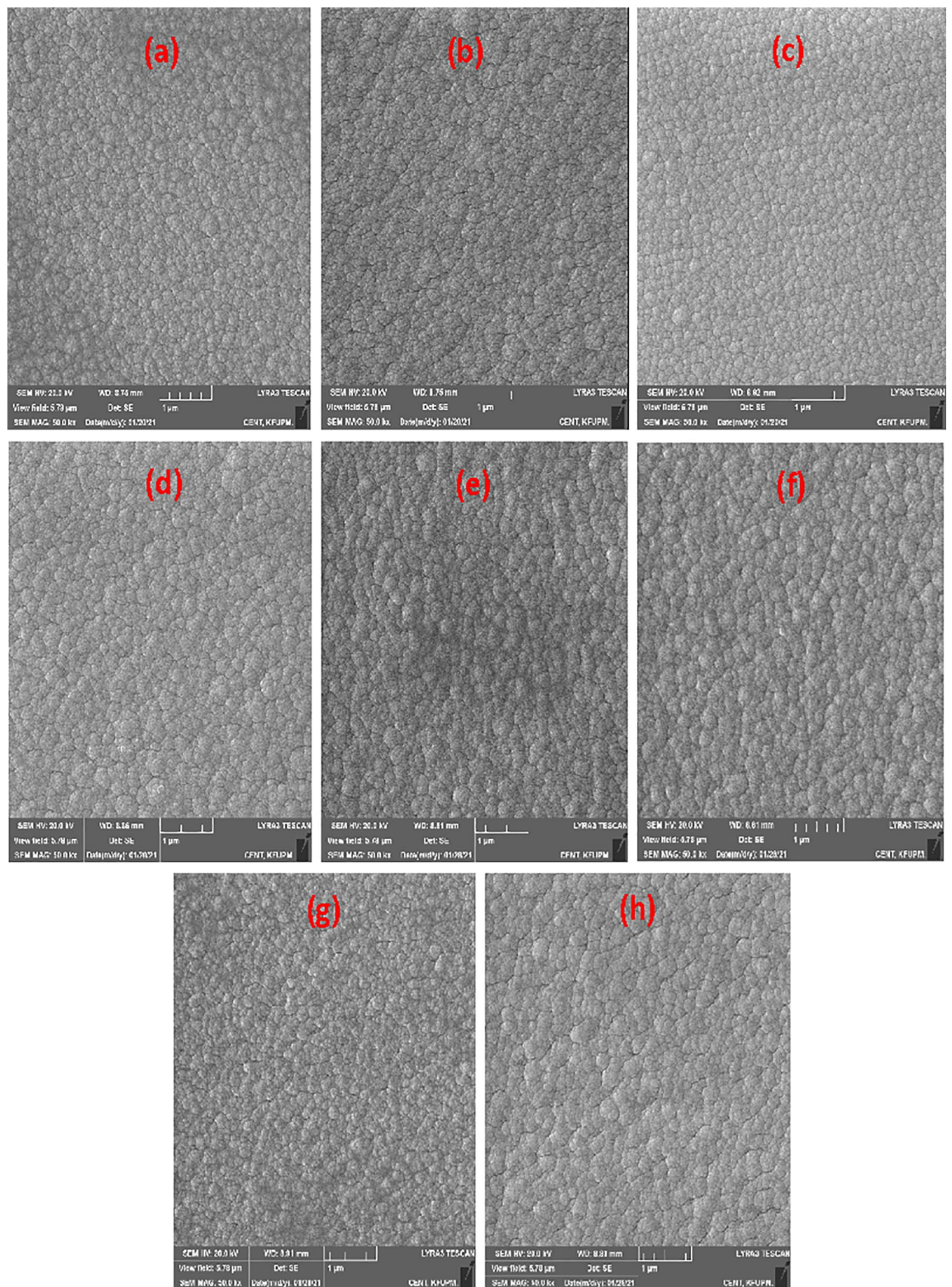


Figure 6. High magnification FESEM micrographs of (a) PN7, (b) PN8, (c) PN9, (d) PN10, (e) PN11, (f) PN12, (g) PN13 and (h) PN14 coatings' top surfaces.

The representative x-ray mapping also shows the alternating multilayer structure of the coatings, the individual Zr and ZrN coatings for coating PN8 are clearly depicted (Fig. 8c,d).

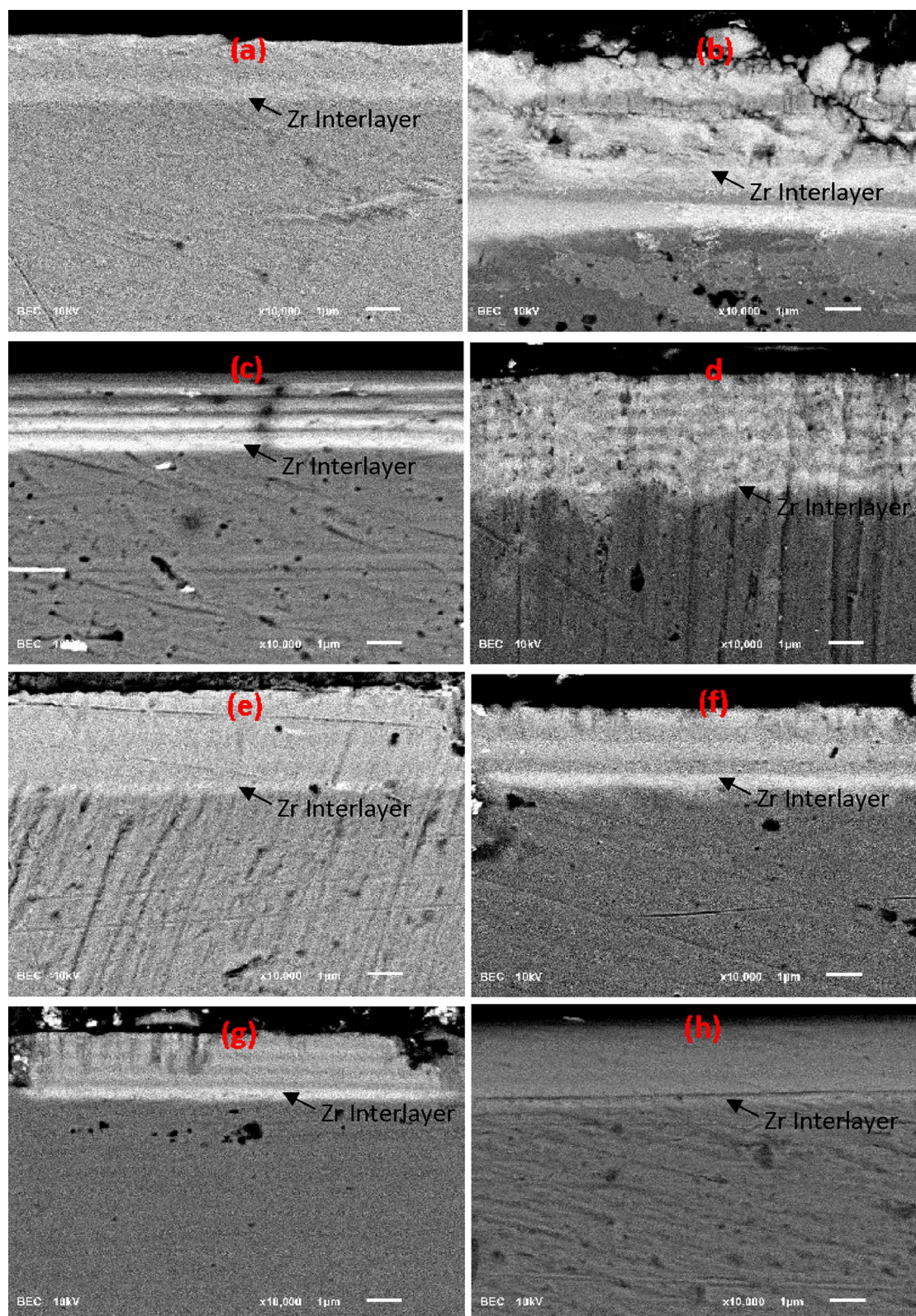


Figure 7. Backscattered electron SEM micrographs of (a) PN7, (b) PN8, (c) PN9, (d) P10, (e) PN11, (f) PN12, (g) PN13 and (h) PN14 coatings' cross-section.

XRD analysis. ZrN is a refractory ceramic substance with a high melting point. It is covalently bonded and has fcc cubic structure. ZrCN forms a quasi-binary solid solution when C and N atoms occupy the octahedral

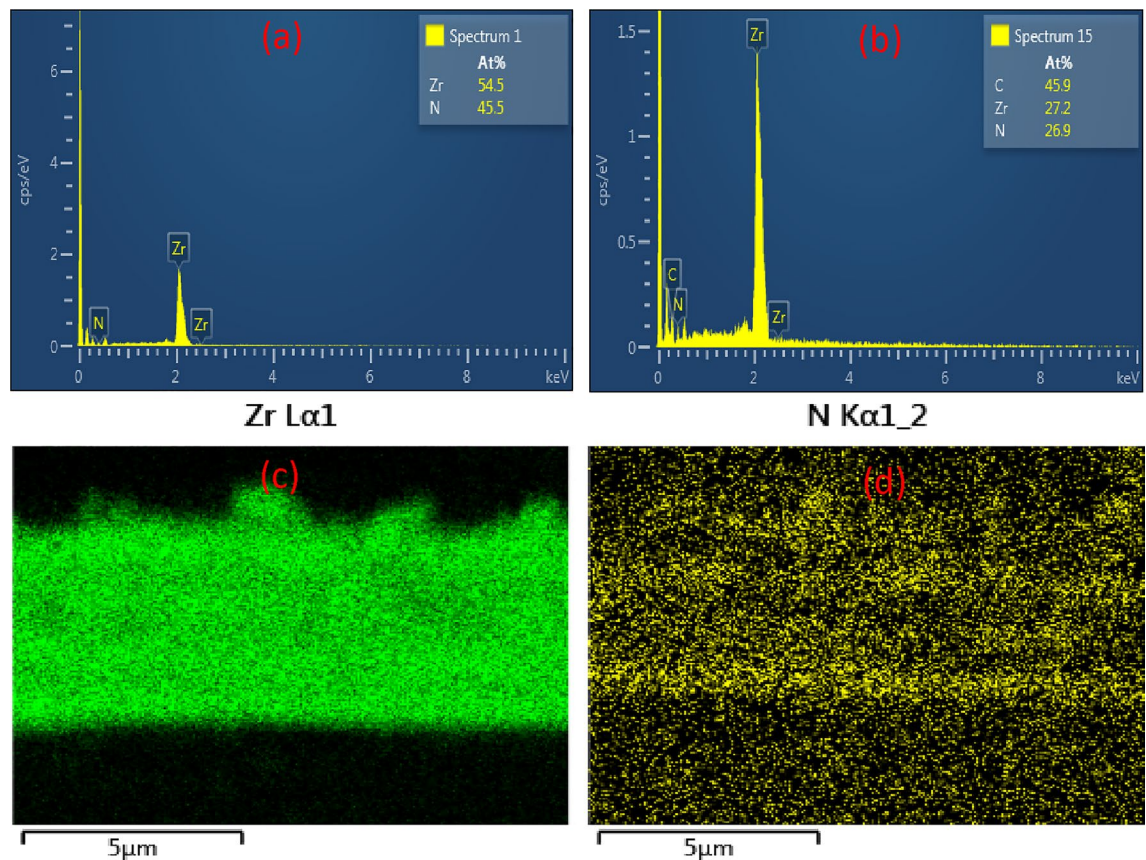


Figure 8. EDS spectra of (a) PN8 & (b) PN12 and X-ray maps of (c) Zr and (d) N for PN8.

interstitial sites⁷⁹. Figure 9 shows the x-ray diffraction spectra obtained from all the multilayer coatings. The spectra match that of an analogous coating described in a recent study^{94,95}, with obvious (fcc) ZrC, Zr₂CN and ZrN, peaks that are almost homogeneous. The standard peak positions of (fcc)-ZrC (ICCD: 00-035-0784), (fcc)-Zr₂CN (ICSD: 01-071-6065) and (fcc)-ZrN (ICCD: 00-035-0753) are plotted as dashed lines. All the coatings peaks were in agreement with the standard ZrN and Zr₂CN. All the coatings exhibited preference for (111) plane. The (220) planes also exhibited a high peak. The (111) plane have been reported as the preferred orientations for ZrN and Zr₂CN coatings^{17,21,38,78}. Other planes that showed low-intensity peaks were planes (200) and (311).

The ZrN/ZrCN coatings had smaller grain size than the Zr/ZrN coatings, this corresponds to the surface morphology of the coatings as observed in the FESEM micrographs (Fig. 6). This is because the carbon atoms in coatings limit grain growth, resulting in tiny grain size. Also in general, the coatings of 3 μm thickness had larger grain size than the ones in 2 μm thickness, this is a consequence of the prolonged deposition times for the coatings of 3 μm thickness as against the 2 μm ones (Table 3).

AFM analysis. The 2D AFM images of all the coatings are shown in Fig. 10. Just as it was observed in the SEM, all the coatings showed compact, uniform and dense morphology of fine spherical grains with the 3 μm coatings appearing more compact, coarse and having grains of larger size than the 2 μm coatings. Also, the 3 μm coatings have larger average roughness (Ra) value than the 2 μm coatings. The larger average roughness value of the 3 μm coatings as against the 2 μm coatings is a consequence of increased clustering and packing which leads to increase vertical size of grains⁹⁶.

Nanoindentation. All nanoindentation tests of all coatings were performed at two different loads (10 & 20 mN). After which, the load (change in applied normal force) vs displacement (depth of penetration) of the indenter over time was plotted. For the same indent, the normal force was plotted vs penetration depth. For all coating compositions, depth of penetration increases with load, ranging from 145 nm (for ZrN/ZrCN) to 435 nm (for Zr/ZrN). The indenter penetration depth for ZrN/ZrCN coatings was within the ideal range (10% of coating thickness). Whereas the Zr/ZrN coatings have penetration depths ranging from 11 to 20% of the coating thickness. This is owing to the fact that Zr/ZrN coatings have lower hardness. The Oliver & Pharr (O & P) method was used to calculate the elastic modulus and nanoindentation hardness from the plots^{62,63}. Figure 11 shows bar charts of nanohardness and elastic modulus plotted for each coating mixture at loads of 10 and 20 mN.

Hardness is controlled by many factors such as preferred orientation, residual stress, grain size, defect density, stoichiometry and structure of the coatings which is turn depend largely on film growth conditions and process

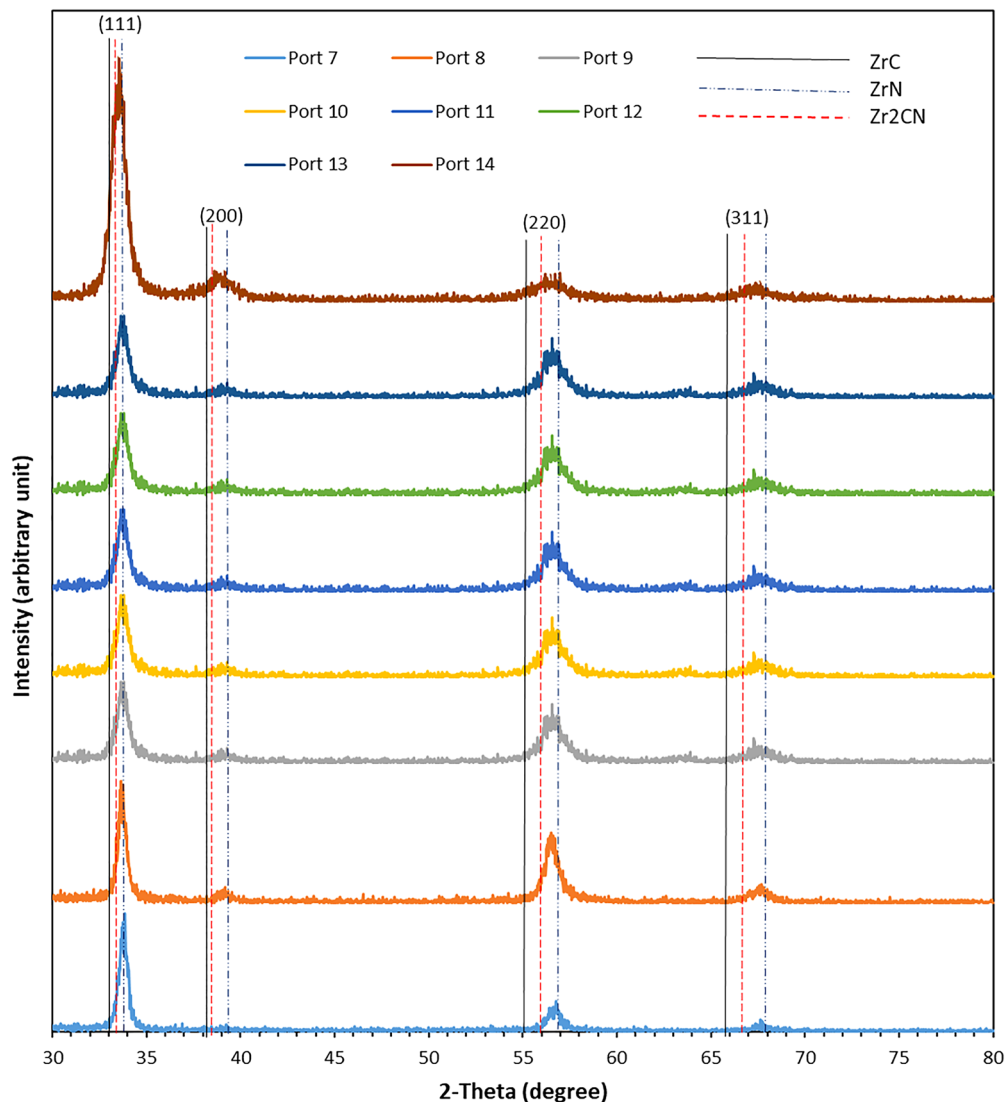


Figure 9. Obtained XRD spectra obtained for (a) PN7, (b) PN8, (c) PN9, (d) P10, (e) PN11, (f) PN12, (g) PN13, and (h) PN14 coatings (the Zr, ZrN and Zr₂CN coatings compositions are identified).

parameters including the synthesis technique, substrate bias, growth temperature, etc.⁹⁷ Fig. 11a shows that the Zr/ZrN multilayer coatings generally have lower hardness values as compared to the ZrN/ZrCN coatings where sample PN12 (3 μm , ZrN/ZrCN multilayer coating having individual layer of each 500 nm in thickness) exhibited the highest hardness of 29.82 and 26.62 GPa at loads of 10 and 20 mN, respectively. Whereas, the 2 μm Zr/ZrN multilayer coating with individual layer thickness 250 nm (sample PN9) exhibited the least hardness of 9.99 and 8.18 GPa at loads of 10 and 20 mN, respectively. The presence of carbon in the ZrN/ZrCN coatings makes the ZrN/ZrCN coatings denser and compact as observed in the FESEM images (Fig. 6). It has been reported the denser and more compact a coating the harder it is^{1,98,99}. As explained above the introduction of carbon leads to dense, firm, smooth and small grain size morphology. High hardness values are achieved for highly dense and nanocrystalline coatings. This is because a highly dense nanostructured coating inhibits sliding or rotation of crystallites due to the lack of free space, thus giving rise to high hardness values⁹⁷. Also for both multilayer coating types, the hardness decreases with decrease in bilayer thickness (Fig. 11a). The influence of the substrate on hardness measurements is reduced by keeping the indent displacement to 10% of the coating thickness. In contrast, a small indent could be comparable in size to the sample surface roughness, reducing measurement accuracy. As a result, there will be a discrepancy in the measurement results. To avoid this, the penetration depth must be at least 20 times the roughness of the surface. The majority of the time, a compromise between these two competing conditions is reached. The change from an elastic to an elastic/plastic state in the indented region makes measurement difficult at low stresses⁶². Soft films on hard surfaces typically increase in hardness as the indenter penetration depth increases, whereas hard films on soft substrates frequently decrease in hardness as displacement increases. For all the coatings, the hardness value was observed to decrease with increase in load from 10 to 20 mN. Stainless steel substrate influence on coating hardness at both load 10 and 20 mN has been

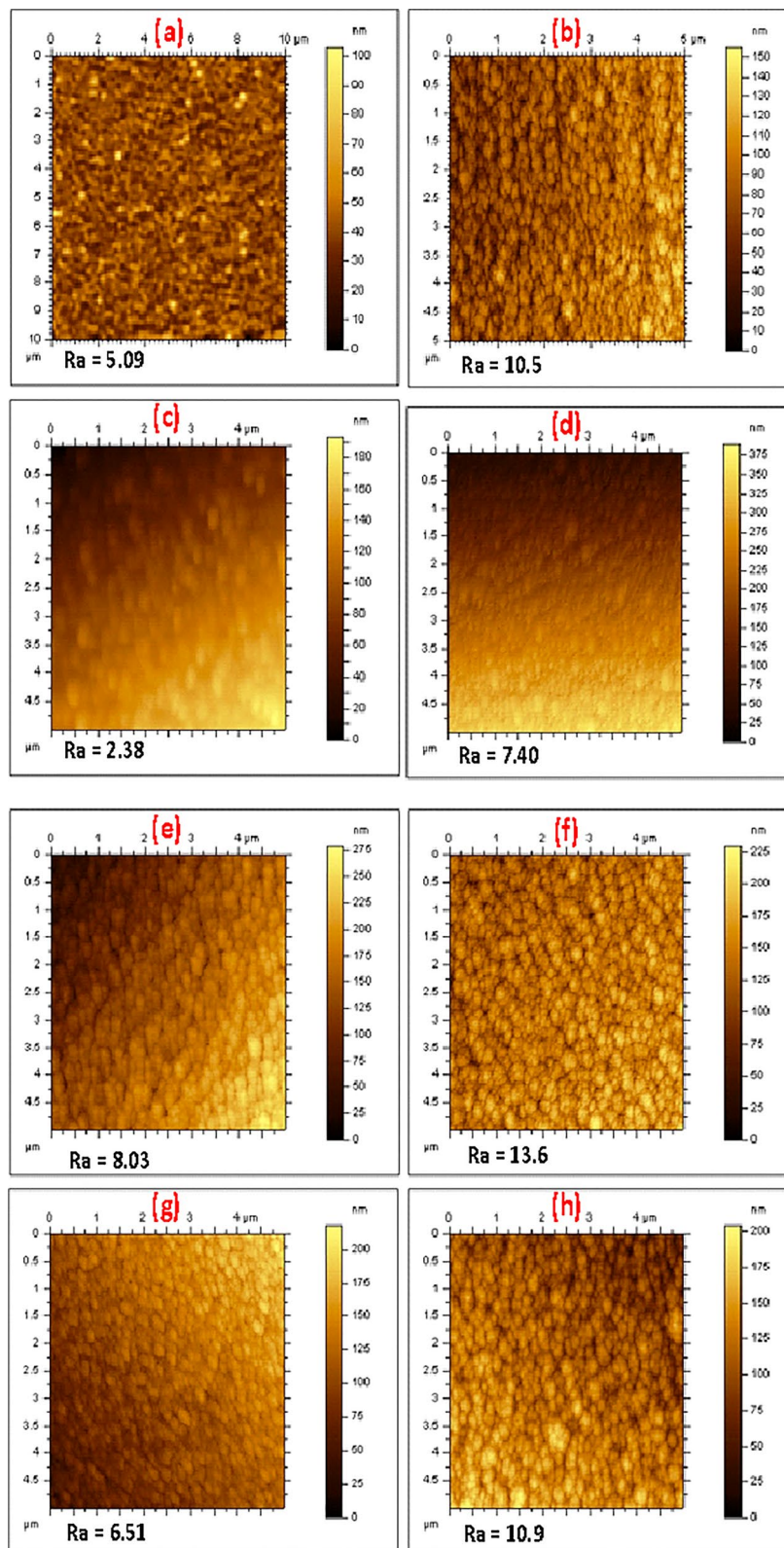


Figure 10. 2D AFM images obtained from the top surfaces (5 × 5 μm area) of (a) PN7, (b) PN8, (c) PN9, (d) PN10, (e) PN11, (f) PN12, (g) PN13, (h) PN14 multilayer coatings. The quoted Ra value for each coating is the average of Ra values obtained at 11 different points across the 5 × 5 μm area.

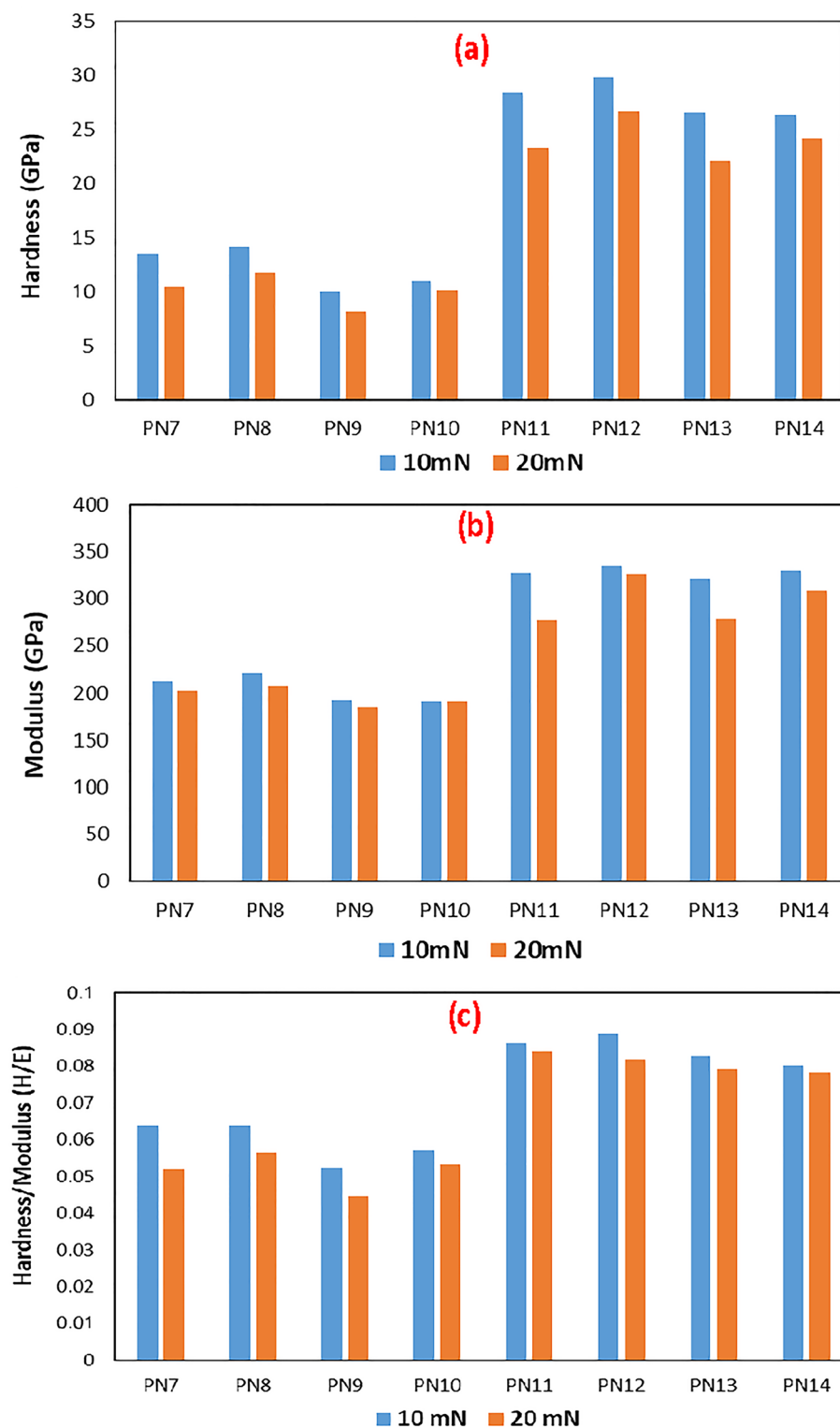


Figure 11. Bar charts showing values of (a) hardness, (b) elastic modulus and (c) hardness/elastic modulus (H/E) values for all the studied multilayer coatings.

discussed in a previous study⁷⁸. It was reported there that the hardness of the substrate was measured as 2.10 GPa. The substrate was reported to have little effect on the coatings hardness at 10 mN while at the 20 mN load, the substrate showed a more significant effect on the coating hardness, it reduced the coating hardness at this

load. Also the effect of substrate on coating hardness was also reported to reduce with coating thickness⁷⁸. All these suggest that the underlying stainless steel substrate possessed a much lesser hardness than the coatings.

Similar trends just as in the case of hardness was observed for elastic modulus. The Zr/ZrN multilayer coatings generally have lower values of elastic modulus as compared to the ZrN/ZrCN coatings where sample PN12 (3 µm, ZrN/ZrCN multilayer coating having individual layer each 500 nm in thickness) exhibited the highest elastic modulus of 335.3 and 325.2 GPa at load 10 and 20 mN respectively. Whereas, the 2 µm Zr/ZrN multilayer coating with individual layer thickness, 250 nm (sample PN9) showed the lowest elastic modulus of 190.8 and 184.0 GPa at load 10 and 20 mN respectively (Fig. 11b).

It is well understood that hardness is not the only criterion for predicting coating wear, the ratio of hardness to modulus (H/E) which is related to elastic strain to failure and fracture toughness has been proposed as one of the key parameters controlling wear^{100–102}. In fact, the H/E ratio has been shown by some authors to be a more appropriate parameter for predicting wear resistance compared to hardness, which can be regarded as a vital material property that defines wear resistance^{101,102}. Similar to hardness and modulus, the H/E ratio of ZrN/ZrCN multilayer coatings was higher than that of Zr/ZrN coatings, with PN12 coatings showing the highest H/E value and PN9 coatings having the lowest H/E value (Fig. 11c). A high value of H/E suggests a higher fracture toughness. This implies that the ZrN/ZrCN multilayer coatings generally showed higher fracture toughness than the Zr/ZrN multilayer coatings. The higher hardness and H/E ratio of the ZrN/ZrCN coatings as compared to the Zr/ZrN coatings is due to the presence of carbon in the ZrN/ZrCN coatings as explained earlier.

Conclusions

Using a dc magnetron sputtering method and varied N₂ and C₂H₂ flowrates so as to manipulate the coatings nitrogen and carbon contents, Zr/ZrN and ZrN/ZrCN multilayer coatings, each with individual layer thicknesses of 250 and 500 nm and coatings thicknesses of 2 and 3 µm were deposited on 316L stainless steel. The coatings morphology and microstructure were investigated by high resolution FESEM, BEI, EDS, XRD and AFM techniques. Nanoindentation method was employed to measure the hardness and modulus of the coatings. The ratio of hardness to modulus (H/E) which is related to elastic strain to failure was also employed in the study. The cross-section FESEM images of the coatings reveal the coatings to show mainly growth that is columnar in nature with some tiny grains at the substrate/coating interface. The top surface FESEM images show a homogeneous, compact and dense morphology of fine spherical grains for all the coatings with the ZrN/ZrCN coatings showing more compact and smaller grain size than the Zr/ZrN coatings. The BEIs show alternating bilayers of equal sizes for each coatings. The denser and more compact nature of the ZrN/ZrCN as compared to the Zr/ZrN coatings due to the carbon presence in ZrN/ZrCN resulted in higher hardness, modulus and H/E exhibited by the ZrN/ZrCN coatings. This suggests the ZrN/ZrCN coatings exhibit a higher wear resistance and fracture toughness than the Zr/ZrN coatings. The effective synthesis and excellent characteristics shown by the studied multilayer coatings make them viable candidates for tribological applications.

Received: 18 November 2021; Accepted: 11 March 2022

Published online: 04 April 2022

References

- Guan, X., Wang, Y. & Xue, Q. Effects of constituent layers and interfaces on the mechanical and tribological properties of metal (Cr, Zr)/ceramic (CrN, ZrN) multilayer systems. *Appl. Surf. Sci.* **502**, 144305 (2020).
- González-carmona, J. M. *et al.* Wear mechanisms identification using Kelvin probe force microscopy in TiN, ZrN and TiN/ZrN hard ceramic multilayers coatings. *Ceram. Int.* **46**, 24592–24604 (2020).
- Lopez, G. & Staia, M. H. High-temperature tribological characterization of zirconium nitride coatings. *Surf. Coat. Technol.* **200**, 2092–2099 (2005).
- Staia, M. H. *et al.* Assessment of the mechanical and tribological performance of a ZrN PVD coating. *Surf. Eng.* **35**, 491–500 (2019).
- Derradji, A., Kassabji, F. & Fauchais, P. Preparation of plasma-sprayed coatings of ZrN under a controlled nitrogen atmosphere. *Surf. Coat. Technol.* **29**, 291–301 (1986).
- Duckworth, R. G. High purity sputtered tribological coatings. *Thin Solid Films* **86**, 213–218 (1981).
- Duckworth, R. G. Sputtered coatings for metal finishing. *Trans. IMF Int. J. Surf. Eng. Coat. ISSN* **62**, 109–112 (1984).
- Duckworth, R. G., Harper, R. E. & Jeynes, C. Backscattering analysis of ZrN alloys. *Nucl. Instrum. Methods Phys. Res.* **B15**, 272–274 (1986).
- Azhari, I. E. *et al.* Contact damage investigation of CVD carbonitride hard coatings deposited on cemented carbides. *Int. J. Refract. Metals Hard Mater.* **86**, 105050 (2020).
- Gruss, K. A., Zheleva, T., Davis, R. F. & Watkins, T. R. Characterization of zirconium nitride coatings deposited by cathodic arc sputtering. *Surf. Coat. Technol.* **107**, 115–124 (1998).
- Huang, S., Tong, C., Hsieh, T. & Lee, J. Microstructure and mechanical properties evaluation of cathodic arc deposited CrCN/ZrCN multilayer coatings. *J. Alloy. Compd.* **803**, 1005–1015 (2019).
- Krysinina, O. V. *et al.* Synthesis of single-layer ZrN-coatings using vacuum-arc plasma-assisted deposition with plasma flow filtering. *Russ. Phys. J.* **62**, 106–111 (2019).
- Kuznetsova, T., Lapitskaya, V., Warcholinski, B., Gilewicz, A. & Chizhik, S. Friction and wear of ZrN coatings under conditions of microcontact using atomic-force microscopy. *J. Friction Wear* **41**, 287–294 (2020).
- Meng, Q. N., Wen, M., Qu, C. Q., Hu, C. Q. & Zheng, W. T. Preferred orientation, phase transition and hardness for sputtered zirconium nitride films grown at different substrate biases. *Surf. Coat. Technol.* **205**, 2865–2870 (2011).
- Musil, J. *et al.* Properties of TiN, ZrN and ZrTiN coatings prepared by cathodic arc evaporation. *Mater. Sci. Eng. A* **163**, 211–214 (1993).
- Singh, A. *et al.* Tribological properties of sputter deposited ZrN coatings on titanium modified austenitic stainless steel. *Wear* **280–281**, 22–27 (2012).
- Ramana, J. V., Kumar, S., David, C., Ray, A. K. & Raju, V. S. Characterisation of zirconium nitride coatings prepared by DC magnetron sputtering. *Mater. Lett.* **43**, 73–76 (2000).

18. Simpson, J. C. B. & Earwaker, L. G. Nuclear analysis of zirconium nitride thin films. *Nucl. Instrum. Methods Phys. Res.* **B24**(25), 701–704 (1987).
19. Ingersoll, R. C. Very high rate reactive sputtering of TiN, ZrN and HfN. *Thin Solid Films* **107**, 141–147 (1983).
20. Sue, J. A. & Chang, T. P. Friction and wear behavior of titanium nitride, zirconium nitride and chromium nitride coatings at elevated temperatures. *Surf. Coat. Technol.* **76–77**, 61–69 (1995).
21. Valerini, D. *et al.* Adhesion and wear of ZrN films sputtered on tungsten carbide substrates. *Thin Solid Films* **538**, 42–47 (2013).
22. Valikhani, M. & Chandrashekar, S. An experimental investigation into the comparison of the performance characteristics of TiN and ZrN coatings on split point drills using the static and stochastic models of the force system as a signature. *Int. J. Adv. Manuf. Technol.* **2**, 75–106 (1987).
23. Muboyadzhyan, S. A. Erosion-resistant coatings for gas turbine compressor blades. *Russ. Metall. (Metally)* **2009**, 3–20 (2009).
24. Sue, J. A. & Troue, H. H. *United States Patent (19) U.S. Patent.* (1989).
25. Lammel, S., Ion, D. I., Roeper, J. & Malenka, R. C. Projection-specific modulation of dopamine neuron synapses by aversive and rewarding stimuli. *Neuron* **70**, 855–862 (2011).
26. Pilloud, D., Dehlinger, A. S., Pierson, J. F., Roman, A. & Pichon, L. Reactively sputtered zirconium nitride coatings : Structural, mechanical, optical and electrical characteristics. *Surf. Coat. Technol.* **174–175**, 338–344 (2003).
27. Patsalas, P. Zirconium nitride: A viable candidate for photonics and plasmonics ?. *Thin Solid Films* **688**, 137438 (2019).
28. Davidson, J. A. & Germantown, T. *United States Patent (19).* (1996).
29. Wu, Z., Wu, Y. & Wang, Q. A comparative investigation on structure evolution of ZrN and CrN coatings against ion irradiation. *Heliyon* **5**, e01370 (2019).
30. Orlova, E. A. *et al.* Formation and investigation of nitride fuel compatible protective coatings on ferrite–martensite steel. *At. Energ.* **105**, 269–274 (2008).
31. Bhattacharya, S. *et al.* Nanocrystalline ZrN thin film development via atomic layer deposition for U-Mo powder. *J. Nucl. Mater.* **526**, 151770 (2019).
32. Maksakova, O. V. *et al.* Nanoscale architecture of (CrN_xZrN_{1-x})₂ nanocomposite coatings—Microstructure, composition, mechanical properties and first-principles calculations. *J. Alloys Compds* **831**, 154808 (2020).
33. Kuznetsova, T. A. *et al.* The influence of the zirconium sublayer thickness on the surface microstructure of the magnetron ZrN coatings. The influence of the zirconium sublayer thickness on the surface microstructure of the magnetron ZrN coatings. *J. Phys. Conf. Ser.* **1281**, 012046 (2019).
34. Mareus, R., Mastail, C., Anğay, F., Brunetière, N. & Abadias, G. Surface & coatings technology study of columnar growth, texture development and wettability of reactively sputter-deposited TiN, ZrN and HfN thin films at glancing angle incidence. *Surf. Coat. Technol.* **399**, 126130 (2020).
35. Huang, J., Kuo, K. & Yu, G. Oxidation behavior and corrosion resistance of vacuum annealed ZrN-coated stainless steel. *Surf. Coat. Technol.* **358**, 308–319 (2019).
36. Zhu, F. *et al.* Surface & coatings technology microstructure and Young’s modulus of ZrN thin film prepared by dual ion beam sputtering deposition. *Surf. Coat. Technol.* **374**, 997–1005 (2019).
37. Pei, C. *et al.* Corrosion inhibition behaviors of ZrN x thin films with varied N vacancy concentration. *Vacuum* **162**, 28–38 (2019).
38. Roman, D. *et al.* Effect of deposition temperature on microstructure and corrosion resistance of ZrN thin films deposited by DC reactive magnetron sputtering. *Mater. Chem. Phys.* **130**, 147–153 (2011).
39. Matsuoka, M., Isotani, S., Sucasaire, W., Kuratani, N. & Ogata, K. X-ray photoelectron spectroscopy analysis of zirconium nitride-like films prepared on Si (100) substrates by ion beam assisted deposition. *Surf. Coat. Technol.* **202**, 3129–3135 (2008).
40. Ma, C. H., Huang, J. H. & Chen, H. A study of preferred orientation of vanadium nitride and zirconium nitride coatings on silicon prepared by ion beam assisted deposition. *Surf. Coat. Technol.* **133–1345**, 289–294 (2000).
41. Kuznetsova, T. *et al.* Applied surface science the influence of nitrogen on the morphology of ZrN coatings deposited by magnetron sputtering. *Appl. Surf. Sci.* **522**, 146508 (2020).
42. Mahmood, K., Bashir, S., Akram, M. & Hayat, A. Surface, structural, electrical and mechanical modifications of pulsed laser deposited ZrN thin films by implantation of MeV carbon ions. *Nuclear Inst. Methods Phys. Res. B* **448**, 61–69 (2019).
43. Rauchenwald, E., Lessiak, M., Weissenbacher, R. & Haubner, R. Author’s accepted manuscript. *Ceram. Int.* **45**, 9410–9414 (2019).
44. Oliveira, C. I. *et al.* Zr-O-N coatings for decorative purposes: Study of the system stability by exploration of the deposition parameter space. *Surf. Coat. Technol.* **343**, 30–37 (2018).
45. Muneshwar, T. & Cadien, K. Applied surface science comparing XPS on bare and capped ZrN films grown by plasma enhanced ALD: Effect of ambient oxidation. *Appl. Surf. Sci.* **435**, 367–376 (2018).
46. Singh, A. *et al.* Applied surface science influence of nitrogen flow rate on microstructural and nanomechanical properties of Zr-N thin films prepared by pulsed DC magnetron sputtering. *Appl. Surf. Sci.* **280**, 117–123 (2013).
47. Berndt, H., Zeng, A.-Q., Stock, H.-R. & Mayr, P. Zirconium carbonitride films produced by plasma-assisted metal organic chemical vapour deposition. *Surf. Coat. Technol.* **74–75**, 369–374 (1995).
48. Caillet, M., Ayedi, H. F. & Besson, J. Tudedelac rro i nderev tement r fractaire sur lezirconium III. Oxidation parlavapeurdeauderev@tementsdenitrueretdecarbonitrurede zirconium. *J. Less-Common Met.* **58**, 37–46 (1978).
49. Sintsova, I. T. & Kbzloovskii, L. V. Mechanical properties and corrosion resistance of steels with titanium and zirconium carbonitride coatings. *Prot. Met.* **6**, 567–570 (1970).
50. Claveria, I. *et al.* Enhancement of tribological behavior of rolling bearings by applying a multilayer ZrN/ZrCN coating. *Coatings* **9**, 434 (2019).
51. Grigore, E., Ruset, C., Li, X. & Dong, H. Surface & coatings technology zirconium carbonitride films deposited by combined magnetron sputtering and ion implantation (CMSII). *Surf. Coat. Technol.* **204**, 1889–1892 (2010).
52. Yao, S., Su, Y. & Lai, Y. Carbonitride coatings doped with W, Ti, Zr, or Cr. *Materials* **10**, 1–16 (2017).
53. Calderon, S. V. *et al.* Nano-galvanic coupling for enhanced Ag⁺ release in ZrCN-Ag films: Antibacterial application. *Surf. Coat. Technol.* <https://doi.org/10.1016/j.surfcoat.2016.04.019> (2016).
54. Calderon, S. V., Cavaleiro, A. & Carvalho, S. Electrochimica acta electrochemical response of ZrCN-Ag-a (C, N) coatings in simulated body fluids. *Electrochim. Acta* **176**, 898–906 (2015).
55. Ferreri, I. *et al.* Silver activation on thin films of Ag–ZrCN coatings for antimicrobial activity. *Mater. Sci. Eng. C* **55**, 547–555 (2015).
56. Wang, L. *et al.* Mechanism of fixation of CO₂ in the presence of hydroxyl-functionalized quaternary ammonium salts. *J. CO₂ Util.* **10**, 113–119 (2015).
57. Ferreri, I. *et al.* Study of the effect of the silver content on the structural and mechanical behavior of Ag–ZrCN coatings for orthopedic prostheses. *Mater. Sci. Eng. C* **42**, 782–790 (2014).
58. Calderon, S. V., Oliveira, J. C., Evaristo, M., Cavaleiro, A. & Carvalho, S. Applied surface science prediction of optimized composition for enhanced mechanical and electrochemical response of Zr-C-N-Ag coatings for medical devices. *Appl. Surf. Sci.* **320**, 570–580 (2014).
59. Calderon, S. V., Galindo, R. E., Oliveira, J. C., Cavaleiro, A. & Carvalho, S. Surface & coatings technology Ag⁺ release and corrosion behavior of zirconium carbonitride coatings with silver nanoparticles for biomedical devices. *Surf. Coat. Technol.* **222**, 104–111 (2013).

60. Calderon, S. V., Cavaleiro, A. & Carvalho, S. Applied surface science chemical and structural characterization of Zr C N Ag coatings : XPS, XRD and Raman spectroscopy. *Appl. Surf. Sci.* **346**, 240–247 (2015).
61. *Concentrated Solar Thermal Energy Technologies*. (Springer, 2018).
62. Vepřek, S. & Vepř, S. The search for novel, superhard materials. *J. Vac. Sci. Technol. A* **17**, 2401–2419 (1999).
63. Vladescu, A. *et al.* Influence of bilayer period on the characteristics of nanometre-scale ZrN/TiAlN multilayers. *J. Nanosci. Nanotechnol.* **8**, 717–721 (2008).
64. Yashar, P. C. & Sproul, W. D. Nanometer scale multilayered hard coatings. *Vacuum* **55**, 179–190 (1999).
65. Hovsepian, PEh., Lewis, D. B. & Munz, W. D. Recent progress in large scale manufacturing of multilayer/superlattice hard coatings. *Surf. Coat. Technol.* **133–134**, 166–175 (2000).
66. Musil, J. Hard and superhard nanocomposite coatings. *Surf. Coat. Technol.* **125**, 322–330 (2000).
67. Imbeni, V., Martini, C., Lanzoni, E., Poli, G. & Hutchings, I. M. Tribological behaviour of multi-layered PVD nitride coatings. *Wear* **251**, 997–1002 (2001).
68. Vereschaka, A. *et al.* Influence of thickness of multilayered Zr-ZrN- (ZrCrNbAl) N on tool life of metal cutting tools at various cutting speeds. *Coatings* **8**, 1–9 (2018).
69. Chen, S. *et al.* Surface & coatings technology the effect of Cr/Zr chemical composition ratios on the mechanical properties of CrN/ZrN multilayered coatings deposited by cathodic arc deposition system. *Surf. Coat. Technol.* **231**, 247–252 (2013).
70. Guan, C. X. *et al.* Microstructures and properties of Zr/CrN multilayer coatings fabricated by multi-arc ion plating. *Tribol. Int.* **106**, 78–87 (2017).
71. Braic, V. *et al.* TiAlN_TiAlZrN multilayered hard coatings for enhanced performance of HSS drilling tools. *Surf. Coat. Technol.* **204**, 1925–1928 (2010).
72. Braic, M., Braic, V., Balaceanu, M., Pavelescu, G. & Vladescu, A. Plasma deposition of alternate TiN/ZrN multilayer hard coatings. *J. Optoelectron. Adv. Mater.* **5**, 1399–1404 (2003).
73. Wei, C. *et al.* An overview of laser-based multiple metallic material additive manufacturing: from macro- to micro-scales. *Int. J. Extreme Manuf.* **3**, 012003 (2020).
74. Huang, Y. *et al.* Investigation of melt-growth alumina/aluminum titanate composite ceramics prepared by directed energy deposition. *Int. J. Extreme Manuf.* **3**(3), 035101–3 (2021).
75. Vladescu, A. *et al.* Nanostructured multilayer nitride coatings for biocompatible materials. *Eur. Cells Mater.* **11**, 36 (2006).
76. Greene, J. E. Review Article : Tracing the recorded history of thin-film sputter deposition : From the 1800s to 2017. *Vac. Surf. Films* **35**, 204 (2019).
77. Silva, E. *et al.* Structure–property relations in ZrCN coatings for tribological applications. *Surf. Coat. Technol.* **205**, 2134–2141 (2010).
78. Ul-Hamid, A. Synthesis, microstructural characterization and nanoindentation of Zr, Zr-nitride and Zr-carbonitride coatings deposited using magnetron sputtering. *J. Adv. Res.* **29**, 107–119 (2020).
79. Saha, R. & Nix, W. D. Effects of the substrate on the determination of thin film mechanical properties by nanoindentation. *Acta Mater.* **50**, 23–38 (2002).
80. Saha, R. & Nix, W. D. Solt films on hard substrates—Nanoindentation of tungsten films on sapphire substrates. *Mater. Sci. Eng., A* **319–321**, 898–901 (2001).
81. Rother, B. & Dietrich, D. A. A new valuation of the classical hardness definition and consequences for mechanical characterizations of thin films. *Surf. Coat. Technol.* **74–75**, 614–617 (1995).
82. Schiffmann, K. I. Determination of fracture toughness of bulk materials and thin films by nanoindentation: Comparison of different models. *Philos. Mag.* **91**, 1163–1178 (2011).
83. Oliver, G. M. & Pharr, W. C. Measurement of thin film mechanical properties using nanoindentation. *MRS Bull.* **17**, 28–33 (1992).
84. Pharr, G. M. Measurement of mechanical properties by ultra-low load indentation. *Mater. Sci. Eng. A* **253**, 151–159 (1998).
85. Rother, B., Lunow, T. & Leonhardt, G. Interface strength of titanium nitride coatings on hardened high-speed steel. *Surf. Coat. Technol.* **71**, 229–232 (1995).
86. Musil, J., Kunc, F., Zeman, H. & Poláková, H. Relationships between hardness, Young’s modulus and elastic recovery in hard nanocomposite coatings. *Surf. Coat. Technol.* **154**, 304–313 (2002).
87. Friedrich, C., Berg, G., Broszeit, E. & Berger, C. Measurement of the hardness of hard coatings using a force indentation function. *Thin Solid Films* **290–291**, 216–220 (1996).
88. Karvanková, P., Männling, H. D., Eggs, C. & Vepřek, S. Thermal stability of ZrN-Ni and CrN-Ni superhard nanocomposite coatings. *Surf. Coat. Technol.* **146–147**, 280–285 (2001).
89. Depla, D., Mahieu, S. & Greene, J. E. Sputter deposition processes. in *Handbook of Deposition Technologies for Films and Coatings*. Vol. 281. 253–296. (William Andrew Applied Science Publishers, 2010).
90. Thompson, C. V. & Carel, R. Texture development in polycrystalline thin films. *Mater. Sci. Eng. B* **32**, 211–219 (1995).
91. Thornton, J. A. High rate thick film growth. *Annu. Rev. Mater. Sci.* **7**, 239 (1977).
92. Liu, C. P. & Yang, H. G. Systematic study of the evolution of texture and electrical properties of ZrNx thin films by reactive DC magnetron sputtering. *Thin Solid Films* **444**, 111–119 (2003).
93. Ul-hamid, A. The effect of deposition conditions on the properties of Zr-carbide, Zr-nitride and Zr-carbonitride coatings—A review. *Mater. Adv.* **1**, 988–1011 (2020).
94. Manier, C. A., Ziegele, H., Barriga, J., Goikoetxea, J. & Woydt, M. Zirconium-based coatings in highly stressed rolling contacts as alternative solution to DLC and ta-C coatings. *Wear* **269**, 770–781 (2010).
95. Frank, F., Tkadletz, M., Czettel, C. & Schalk, N. Microstructure and mechanical properties of zrn, zrcn and zrc coatings grown by chemical vapor deposition. *Coatings* **11**, 1–13 (2021).
96. Niu, E. W. *et al.* Influence of substrate bias on the structure and properties of ZrN films deposited by cathodic vacuum arc. *Mater. Sci. Eng. A* **460–461**, 135–139 (2007).
97. Ul-Hamid, A. Microstructure, properties and applications of Zr-carbide, Zr-nitride and Zr-carbonitride coatings: A review. *Mater. Adv.* **1**, 1012–1037 (2020).
98. Craciun, V., McCumiskey, E. J., Hanna, M. & Taylor, C. R. Very hard ZrC thin films grown by pulsed laser deposition. *J. Eur. Ceram. Soc.* **33**, 2223–2226 (2013).
99. Balaceanu, M. *et al.* Characterization of Zr-based hard coatings for medical implant applications. *Surf. Coat. Technol.* **204**, 2046–2050 (2010).
100. Ni, W. *et al.* Effects of the ratio of hardness to Young’s modulus on the friction and wear behavior of bilayer coatings. *Appl. Phys. Lett.* **85**, 4028–4030 (2004).
101. Oberle, T. L. Wear of metals. *J. Met.* **3**, 438–439 (1951).
102. Leyland, A. & Matthews, A. On the significance of the H/E ratio in wear control: a nanocomposite coating approach to optimised tribological behaviour. *Wear* **246**, 1–11 (2000).

Acknowledgements

Support provided by the Deanship of Research Oversight and Coordination at the King Fahd University of Petroleum & Minerals, Dhahran 31261, Saudi Arabia through project number SB191053 is gratefully acknowledged.

Author contributions

Sole author contribution. All contribution by single author.

Competing interests

The author declares no competing interests.

Additional information

Correspondence and requests for materials should be addressed to A.U.-H.

Reprints and permissions information is available at www.nature.com/reprints.

Publisher's note Springer Nature remains neutral with regard to jurisdictional claims in published maps and institutional affiliations.



Open Access This article is licensed under a Creative Commons Attribution 4.0 International License, which permits use, sharing, adaptation, distribution and reproduction in any medium or format, as long as you give appropriate credit to the original author(s) and the source, provide a link to the Creative Commons licence, and indicate if changes were made. The images or other third party material in this article are included in the article's Creative Commons licence, unless indicated otherwise in a credit line to the material. If material is not included in the article's Creative Commons licence and your intended use is not permitted by statutory regulation or exceeds the permitted use, you will need to obtain permission directly from the copyright holder. To view a copy of this licence, visit <http://creativecommons.org/licenses/by/4.0/>.

© The Author(s) 2022